ABSTRACT

EXPERIMENTAL STUDIES OF ISOBARIC QUINTETS

By

Arno George Ledebuhr

The mass excesses of the lowest T=2 states in the nuclei ^{24}Al, ^{8}Be, and ^{8}Li have been determined.

The highly proton-rich nucleus ^{24}Si has been produced via the ^{24}Mg(^{3}He,3n) reaction. A cryogenic helium jet and a recoil time-of-flight mass analyzer system were constructed for use in observing short-lived beta-delayed particle emitters. The half-life of ^{24}Si was found to be 103(42) ms, and the energy of the protons de-exciting the T=2 state in the daughter, ^{24}Al, has been measured as 3912.7(37) keV. From detailed consideration of masses in the A=24 completed isobaric quintet, it is concluded that this quintet constitutes a test of the quadratic isobaric multiplet mass equation (IMME) as precise as the mass 9 quartet and that there is, in this case, no significant departure from the equation.

Measurements of the Q values for the reactions ^{10}Be(p,t)^{8}Be(T=2) and ^{10}Be(p,^{3}He)^{8}Li(T=2) have been carried out using an Enge split-pole magnetic spectrograph. Data

were recorded on photographic plates and analyzed using the MSU plate-scanning system. The Q values determined were -27484.3(14) keV and -26821.3(57) keV for the ^{8}Be and ^{8}Li experiments respectively. These measurements have removed the deviation from the quadratic IMME that existed previous to these results.

An analysis of all A=4n isobaric quintets (five complete) for $A \leq 44$ has been carried out. Predictions for missing members have been made using the quadratic IMME. In no case has any significant deviation from the quadratic form of the isobaric multiplet mass equation been found. This leaves only the mass 9 ground state quartet where a known deviation is present and where sources of significant experimental error have probably been eliminated.

EXPERIMENTAL STUDIES OF ISOBARIC QUINTETS

By

Arno George Ledebuhr

A DISSERTATION

Submitted to
Michigan State University
in partial fulfillment of the requirements
for the degree of

DOCTOR OF PHILOSOPHY

Department of Physics

1982

To Sharon,
with all my love

ACKNOWLEDGMENTS

I would first like to thank my advisor, Dr. R.G.H. (Hamish) Robertson for suggesting this thesis project and for helping and guiding me during my graduate school career. Hamish has been a real friend and mentor.

I would also like to thank all the staff at the Cyclotron Laboratory with whom I have worked — both past and present. They have made working (and sometimes living) at the lab more enjoyable for me.

To my fellow graduate students — my nuclear beer companions — I would like to say that your support, our friendship and good times will always be remembered.

Lastly, I would like to thank my wife, Sharon, for her love and companionship, for her patience through the many lonely nights and for all her help in preparing this thesis.

TABLE OF CONTENTS

LIST OF TABLES

LIST OF FIGURES

INTRODUCTION

The isobaric multiplet mass equation (IMME) is a result of first-order perturbation theory, with the assumption that only two-body forces are responsible for charge-dependent effects in nuclei. The equation predicts that the mass excesses ΔM of analog states of an isobaric multiplet can be determined by a three-parameter quadratic equation

$$\Delta M = a + bT_z + cT_z^2.$$

Deviations from the quadratic form of the IMME could be expected if there were charge-dependent many-body nuclear forces, isospin mixing or shifts in unbound levels. These deviations are usually parametrized as cubic or quartic terms in T_z (dT_z^3,eT_z^4). If an isobaric quintet (T=2 multiplet) is used to test this equation, both additional terms can be determined, whereas only one can be determined in a quartet (T=3/2 multiplet).

In a review article by Benenson and Kashy (Be79), an analysis of 22 complete isobaric quartets found that only in one case - the ground state A=9 quartet - was there a significant deviation from the quadratic IMME (d coefficient of 5.8(16) keV). However, mass 9 is also the most accurately measured quartet and one cannot conclude that

this deviation is exceptional without obtaining results of comparable accuracy in other multiplets. Isobaric quintets offer the prospect of improved tests of the IMME.

This dissertation describes measurements which yield a test of the IMME in the A=24 quintet of the same level of precision as the mass 9 quartet. New measurements on the A=8 quintet have removed the slight deviation that existed previous to this work.

The thesis is organized as follows: Chapter One contains a discussion of the theory of the isobaric multiplet mass equation; Chapter Two describes the measurement of the ^{24}Al T=2 level and includes the details of the design of a cryogenic helium jet and recoil time-of-flight mass analyzer system constructed for this measurement; Chapter Three contains the details of the measurements of the lowest T=2 levels in ^{8}Be and ^{8}Li; Chapter Four discusses the A=24 and 8 quintets along with a summary of the remaining A=4n quintets for $A \leq 44$. There are now five completed quintets.

CHAPTER ONE

1.1 Isotopic spin and charge-independence.

Isotopic spin has its origins in the observations of low energy proton scattering which revealed that, neglecting Coulomb effects, the proton-proton (p-p) and proton-neutron (p-n) forces are very similar (Br36,Ca36). These observations led to the hypothesis of the charge-independence of the nuclear force and started the development of isospin as an important quantum number.

The hypothesis of charge-independence is that, neglecting the electromagnetic effects, the force between p-p, p-n and n-n pairs will be identical when these pairs are in the same space and spin states. Because the p-n system is not made of identical particles, there are space and spin configurations available to this system that are not allowed for the p-p and n-n system. It is only those configurations (where the identity of the nucleons does not matter) for which the forces may be compared.

Heisenberg postulated (He32) (shortly after the discovery of the neutron) that the specifically nuclear forces between a pair of protons (p-p) would be the same as that between a pair of neutrons (n-n). The hypothesis, of

the equivalence of the p-p and n-n force, is known as charge-symmetry. This is a less restrictive statement than the one of charge-independence because charge-independence implies charge-symmetry but not vice versa.

The charge-dependent nature of the nuclear force is considered to be due solely to the effects of the electromagnetic interaction. These effects are classified as direct and indirect (He69). The direct part includes the Coulomb force, vacuum polarization effects, the neutron-proton mass difference, and the magnetic forces (such as the spin-orbit force). These direct effects involve no meson exchange between the nucleons and are present even in the absence of hadronic forces.

The indirect charge-dependent effects are present only when there are nuclear forces. These effects, as described by Henley (He69,He81), include the mass difference between the neutral and charged mesons, mass differences of baryons (during two-pion exchange for example), radiative corrections to meson-nucleon coupling constants, meson mixing caused by the electromagnetic interaction, and forces that arise from meson plus photon exchanges.

In isospin formalism, the proton and neutron are opposite projections of the nucleon in isotopic spin space. This is not a projection in physical space as with normal spin but rather a fictitious space used as a convenience. Because of the two-state nature of the nucleon, the same formalism as with spin 1/2 can be applied.

The presence of the isospin quantum number allows for the generalization of the Pauli principle so that the wave function for a system of nucleons must be antisymmetric under interchange of any two nucleons.

The operator t is defined as the isospin operator for an individual nucleon with three cartesian components of t_x, t_y, and t_z. The projection of the t operator is defined as t_z. The neutron is assigned an isospin projection of $t_z=+1/2$ and the proton a projection of $t_z=-1/2$. This is the original (and still-standard) convention that is used in nuclear physics. In particle physics the opposite sign convention is used. The standard nuclear physics notation will be used here.

T is the total isospin operator for the nucleus. This is defined as

$$\vec{T} = \sum_{i=1}^{A} \vec{t}_i \qquad (1\text{-}1)$$

and has a projection given by,

$$T_z = \sum_{i=1}^{A} t_z(i) = (N-Z)/2 \qquad (1\text{-}2)$$

The charge-independent part of the nuclear Hamiltonian H_N commutes with the total isospin operator,

$$[H_N, T^2] = 0 \qquad (1\text{-}3)$$

In the isospin representation, the wave functions of the nuclear Hamiltonian are eigenstates of T and have no T_z dependence. That is

$$H_N \left| \alpha_0, TT_z \right\rangle = E^{(0)}(\alpha_0, T) \left| \alpha_0, TT_z \right\rangle \qquad (1\text{-}4)$$

where α_0 represents all the other quantum numbers (aside from T and T_z) that are necessary to specify the nuclear wave function (such as spin and parity). The energy of these states $E^{(0)}(\alpha_0, T)$ is independent of T_z so there are 2T+1 degenerate states with this energy and with quantum numbers α_0 and T.

These 2T+1 states, all having the same wave functions, will occur in 2T+1 different nuclei. They all have the same total number of nucleons and, therefore, have become known as an isobaric multiplet. The A=8 isobaric quintet (T=2) is shown in Figure 1-1.

For a nucleus with T=1/2, there are two degenerate states with T_z=+1/2 and -1/2. These are called mirror pairs. A state with a T that is larger than the T_z of the nucleus (e.g., a T=1 state in a T_z=Ø nucleus) is known as an analog state, because there exist states in neighboring nuclei that are analogous to it.

The total Hamiltonian for a system of nucleons contains change-dependent terms which do not commute with the isospin operator and, therefore, break the degeneracy of the analog states among a given isobaric multiplet. As mentioned earlier, these terms are considered to be electromagnetic in origin.

Aside from the neutron-proton mass difference, the major contributor to the breaking of the degeneracy among the analog states is the static Coulomb potential. Because the strength of the electromagnetic interaction is

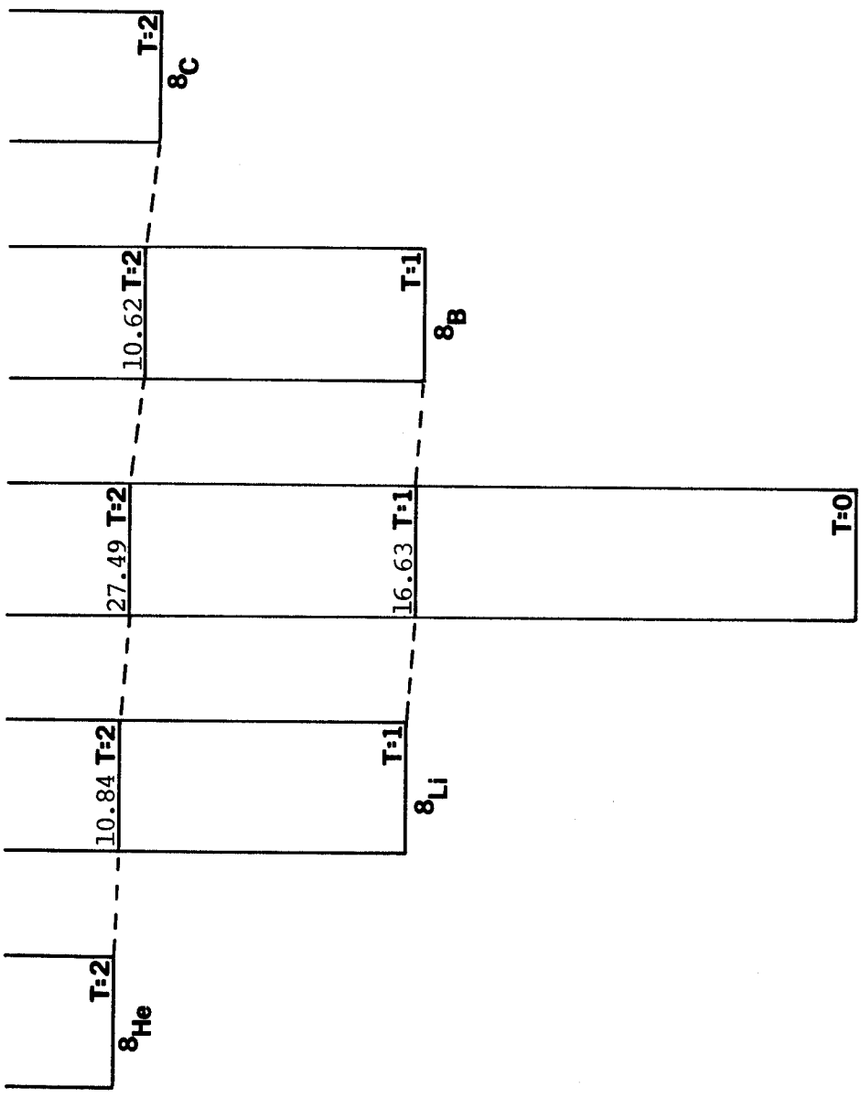

Figure 1-1. The A=8 isobaric (T=2) quintet.

only 1/137 that of the nuclear force, it can be considered as a perturbation on the nuclear force. Perturbation theory can then be used to calculate the splitting between the analog states.

Wigner (Wi57) was the first to show the effect of the Coulomb potential on the mass differences of the analog states. His derivation involved a simple application of the Wigner-Eckart theorem in first-order perturbation theory and produced the well-known isobaric multiplet mass equation (IMME):

$$\Delta M = a + bT_z + cT_z^2 \qquad (1\text{-}5)$$

The crucial decomposition of the Coulomb operator (in isospin representation) into its irreducible parts was first accomplished by MacDonald (Ma55). This explicit decomposition into an isoscalar, isovector and isotensor part allowed for the simple application of the Wigner-Eckart theorem (Wi57).

1.2 Derivation of the IMME.

The total Hamiltonian can be written as the sum of the charge-independent nuclear part H_N, and the charge-dependent electromagnetic part H_C. This latter term can be considered to be due principally to the static Coulomb interaction.

$$H = H_N + H_C \qquad (1\text{-}6)$$

In first-order perturbation theory, the correction to the unperturbed energies $E^{(0)}(\alpha_0,T)$ is

$$E^{(1)}(\alpha_0,T) = \langle \alpha_0 T T_z | H_C | \alpha_0 T T_z \rangle \qquad (1\text{-}7)$$

The Coulomb potential in isospin representation is given by

$$H_C = e^2 \sum_{i<j} \frac{\left(\frac{1}{2} - t_z(i)\right)\left(\frac{1}{2} - t_z(j)\right)}{r_{ij}} \qquad (1\text{-}8)$$

With the stated convention that t_z=1/2 for neutrons and t_z=-1/2 for protons, the $(1/2-t_z(i))(1/2-t_z(j))$ product will then be nonzero only for proton pairs. Multiplying these terms together yields

$$H_C = e^2 \sum_{i<j} \frac{1}{r_{ij}} \left[\frac{1}{4} - \frac{1}{2}\left(t_z(i)+t_z(j)\right) + t_z(i)\,t_z(j)\right] \qquad (1\text{-}9)$$

Inserting the isoscalar $\frac{\vec{t}(i)\cdot\vec{t}(j)}{3}$ into equation 1-9, (Ma55) results in

$$H_C = e^2 \sum_{i<j} \frac{1}{r_{ij}} \left\{\left[\frac{1}{4} + \frac{\vec{t}(i)\cdot\vec{t}(j)}{3}\right] - \left[\frac{t_z(i)+t_z(j)}{2}\right] + \left[t_z(i)\,t_z(j) - \frac{\vec{t}(i)\cdot\vec{t}(j)}{3}\right]\right\} \qquad (1\text{-}10)$$

The first term in brackets is the zeroth component (in cartesian form) of a zero-rank irreducible tensor operator $H_0^{(0)}$. The second and third bracketed terms are the zeroth components (in cartesian form) of rank 1 and rank 2 irreducible tensor operators $H_0^{(1)}$ and $H_0^{(2)}$ respectively. These terms are listed separately as follows,

$$H_0^{(0)} = e^2 \sum_{i<j} \frac{1}{r_{ij}} \left[\frac{1}{4} + \frac{\vec{t}(i)\cdot\vec{t}(j)}{3} \right] ; \quad \Delta T = 0$$

$$H_0^{(1)} = e^2 \sum_{i<j} \frac{1}{r_{ij}} \left[\frac{t_z(i)+t_z(j)}{2} \right] ; \quad \Delta T = 0, \pm 1 \qquad (1\text{-}11)$$

$$H_0^{(2)} = e^2 \sum_{i<j} \frac{1}{r_{ij}} \left[t_z(i)t_z(j) - \frac{\vec{t}(i)\cdot\vec{t}(j)}{3} \right] ; \quad \Delta T = 0, \pm 1, \pm 2$$

The Coulomb operator can now be expressed as

$$H_C = H_0^{(0)} + H_0^{(1)} + H_0^{(2)} \qquad (1\text{-}12)$$

The ΔT's following the explicit forms of the tensor operators, Equation 1-11, show the connections that each operator can make between states of differing isospin. These connections are not important for first-order perturbation theory where only diagonal matrix elements are considered. However, in second-order perturbation, these operators may cause additional energy shifts due to isospin mixing.

The fact that the Coulomb operator is reducible into the zeroth components of these tensors assures that only states with the same T_z values will overlap (i.e., states in the same nucleus).

Application of the Wigner-Eckart theorem yields for the first-order correction to the unperturbed energies

$$E^{(1)}(\alpha_0,T) = \left\langle \alpha_0 T T_z \left| H_c \right| \alpha_0 T T_z \right\rangle = \sum_{k=0}^{2} \left\langle \alpha_0 T T_z \left| H_0^{(k)} \right| \alpha_0 T T_z \right\rangle$$

$$= \sum_{k=0}^{2} \left\langle T k T_z 0 \left| T T_z \right\rangle \right. \left\langle \alpha_0 T \left| \left| H^{(k)} \right| \right| \alpha_0 T \right\rangle \qquad (1\text{-}13)$$

The Clebsch-Gordan coefficients are

$$\left\langle T 0 T_z 0 \left| T T_z \right\rangle \right. = 1$$

$$\left\langle T 1 T_z 0 \left| T T_z \right\rangle \right. = \frac{T_z}{\sqrt{T(T+1)}} \qquad (1\text{-}14)$$

$$\left\langle T 2 T_z 0 \left| T T_z \right\rangle \right. = \frac{3T_z^2 - T(T+1)}{\sqrt{(2T-1)T(T+1)(2T+3)}}$$

Inserting the Clebsch-Gordan coefficients into Equation 1-13 yields

$$E^{(1)}(\alpha_0,T) = \left\langle \alpha_0 T \left| \left| H^{(0)} \right| \right| \alpha_0 T \right\rangle +$$

$$+ \frac{T_z}{\sqrt{T(T+1)}} \left\langle \alpha_0 T \left| \left| H^{(1)} \right| \right| \alpha_0 T \right\rangle + \qquad (1\text{-}15)$$

$$+ \frac{3T_z - T(T+1)}{\sqrt{(2T-1)T(T+1)(2T+3)}} \left\langle \alpha_0 T \left| \left| H^{(2)} \right| \right| \alpha_0 T \right\rangle$$

Rewriting Equation 1-15 in terms of powers of T_z results in

$$E^{(1)}(\alpha_0,T) = \left[\langle\alpha_0 T||H^{(0)}||\alpha_0 T\rangle - \frac{T(T+1)\ \langle\alpha_0 T||H^{(2)}||\alpha_0 T\rangle}{\sqrt{(2T-1)T(T+1)(2T+3)}}\right] +$$

$$+ \left[\frac{\langle\alpha_0 T||H^{(1)}||\alpha_0 T\rangle}{\sqrt{T(T+1)}}\right] T_z + \qquad (1\text{-}16)$$

$$+ \left[\frac{3\ \langle\alpha_0 T||H^{(2)}||\alpha_0 T\rangle}{\sqrt{(2T-1)T(T+1)(2T+3)}}\right] T_z^2$$

The $E^{(1)}(\alpha_0,T)$ is the mass correction to the unperturbed states and is the well-known isobaric multiplet mass equation (Equation 1-5).

$$\Delta M = a + bT_z + cT_z^2 \qquad (1\text{-}17)$$

The neutron-proton mass difference may be accounted for by simply including a sum of the neutron and proton masses in the Hamiltonian.

$$H_{\Delta M} = M_n N + M_p Z \qquad (1\text{-}18)$$

where N+Z=A and M_n is the neutron mass and M_p is the proton mass. The mass difference effect is made more transparent when Equation 1-18 is written in isospin formalism

$$H_{\Delta M} = \sum_{i=1}^{A}\left[M_n\left(\frac{1}{2}+t_z(i)\right) + M_p\left(\frac{1}{2}-t_z(i)\right)\right] \qquad (1\text{-}19)$$

Upon rearrangement this becomes

$$H_{\Delta M} = \left(\frac{M_n+M_p}{2}\right)\left(\sum_{i=1}^{A}\right) + \left(M_n - M_p\right)\sum_{i=1}^{A} t_z(i) \qquad (1\text{-}2\emptyset)$$

which further reduces to

$$H_{\Delta m} = \left(\frac{M_n+M_p}{2}\right)A + \left(M_n - M_p\right)T_z \qquad (1\text{-}21)$$

These terms can then be absorbed into the a and b coefficients of the IMME.

The spin-orbit interaction has been shown by Garvey and Hecht (Ga69,He66) to also be expressible in terms of irreducible tensor operators of rank zero, one and two. So it too will preserve the form of the IMME.

In general, any two-body force will have the form (Ga69)

$$V_{ij} = V_1\left[t_z(i) + t_z(j)\right] + V_2\left[t_z(i)\,t_z(j)\right] \qquad (1\text{-}22)$$

which may be decomposed into a linear combination of irreducible scalar, vector and tensor operators. Hence, the IMME will result from the use of any two-body force in first-order perturbation theory.

1.3 Violations of the IMME.

In second-order perturbation theory, the correction to the energies for the static Coulomb potential is given as (GA69,BA73)

$$E^{(2)}(\alpha_0,T) = \sum_{T'}\sum_{i} \frac{\left|\left\langle \alpha_0 T T_z \left| H_C \right| \alpha_i T' T_z \right\rangle\right|^2}{E^{(0)}(\alpha_0,T) - E^{(0)}(\alpha_i,T')} \qquad (1\text{-}23)$$

(When $T'=T$, then $i\neq 0$.)

where $T'=T,\ T\pm1,\ T\pm2$.

With the application of the Wigner-Eckart theorem, the explicit T_z dependence of this second-order correction can be extracted. Janecke and Garvey (Ja69,Ga69) have shown that the major effect of this higher-order correction is to alter the a, b, and c coefficients. These changes can then be absorbed back into the standard form of the IMME (Equation 1-17). There are, however, terms with a T_z^3 and T_z^4 dependence generated by this expression which result in the "quartic" form of the IMME

$$\Delta M = a + bT_z + cT_z^2 + dT_z^3 + eT_z^4 \qquad (1\text{-}24)$$

These d and e terms, though small relative to a, b, and c, will have the form

$$d \cong \sum_i \frac{\langle \alpha_0 T || H^{(1)} || \alpha_i T' \rangle \langle \alpha_i T' || H^{(2)} || \alpha_0 T \rangle}{E^{(0)}(\alpha_0,T) - E^{(0)}(\alpha_i,T')} \qquad (1\text{-}25)$$

(When $T'=T$, then $i \neq 0$.)

where $T'=T$, $T \pm 1$.

and

$$e \cong \sum_i \frac{\langle \alpha_0 T || H^{(2)} || \alpha_i T' \rangle^2}{E^{(0)}(\alpha_0,T) - E^{(0)}(\alpha_i,T')} \qquad (1\text{-}26)$$

(When $T'=T$, then $i \neq 0$.)

where $T'=T$, $T \pm 1$ and $T \pm 2$.

In order to distinguish between the effects of a charge-dependent, many-body force (which presumably would manifest itself in first-order perturbation theory) over the higher-order effects of a two-body force, detailed shell-model calculations will be required.

Isospin mixing is expected to cause deviations from the IMME. Isospin-forbidden resonance reactions have been used successfully to discover a number of higher T levels in lower T_z nuclei (T=2 states in T_z=Ø nuclei). So isospin admixtures are known to exist and could therefore be responsible for generating relative shifts between multiplet members. Figure 1-2 illustrates the effect of isospin-mixing in both quartets and quintets. For quartets, it is apparent that mixing with lower T levels would primarily produce only changes in the c coefficient. In quintets, however, mixing between T=Ø and T=2 levels in the T_z=Ø nucleus (Ro76) would, by symmetry, produce an even-order eT_z^4.

In the case of the A=8 multiplet, it is known that this state is admixed with a T=Ø state (from the observation of the T=2 state in the T_z=Ø nucleus ^{8}Be, as an isospin forbidden resonance in the ^{6}Li + d reaction). A generation of an e coefficient is seen to occur, both from the qualitative argument shown in Figure 1-2 and from the results of second-order perturbation theory Equation 1-26. Assuming only one T=Ø perturbing state with the same spin and parity as the T=2 state, the e coefficient has the form

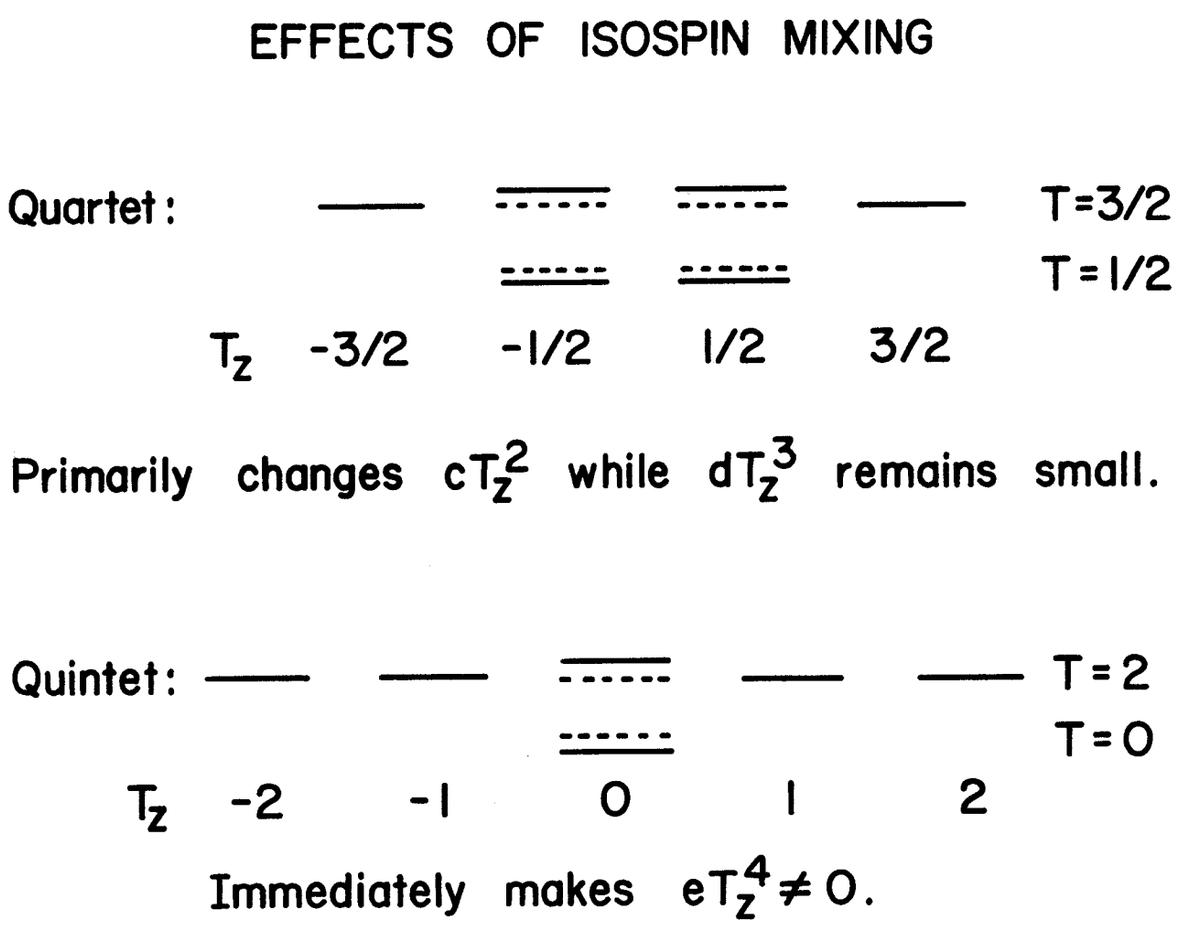

Figure 1-2. Isospin-mixing in quartets and quintets.

$$e = \frac{1}{20} \frac{\langle 2||H^{(2)}||0\rangle^2}{E^{(0)}(2) - E^{(0)}(0)} \qquad (1\text{-}27)$$

where the $\frac{1}{20}$ comes from evaluation of the Clebsch-Gordan coefficients.

For an e coefficient of 1 keV and an off-diagonal matrix element of order 100 keV, the perturbing state must lie within 500 keV of the T=2 state. As of yet this state has not been observed but evaluation of the sign of the e coefficient will determine its position with respect to the T=2 state. Actual observation of this T=0 state would then allow a determination of the size of the off-diagonal Coulomb matrix element.

It has also been suggested that changes in the wave functions between members of a multiplet could cause a deviation from the quadratic IMME. For example, the expansion of the radial wave function due to the effects of the Coulomb repulsion in the proton-rich member of a multiplet could cause a change in the calculated expection value, and hence a change in the relative separation of the levels. However, calculations have shown (Be70,Be77) that the major change occurs in the b and c coefficients and only small d and/or e coefficients are generated. The change to the b and c coefficients is absorbed back into the IMME without causing a significant deviation.

For a complete quintet the five coefficients of the quartic IMME are completely specified:

$$
\begin{aligned}
a &= M_0 \\
b &= \tfrac{1}{12}[8(M_1-M_{-1})-(M_2-M_{-2})] \\
c &= \tfrac{1}{8}[16(M_1+M_{-1})-(M_2+M_{-2})-30M_0] \qquad (1\text{-}28) \\
d &= \tfrac{1}{12}[(M_2-M_{-2})-2(M_1-M_{-1})] \\
e &= \tfrac{1}{24}[(M_2+M_{-2})-4(M_1+M_{-1})+6M_0].
\end{aligned}
$$

From these expressions it is apparent that the coefficients are more sensitive to the inner members of the multiplet and therefore accurate determination of these are necessary for a precise test of the IMME.

CHAPTER TWO

2.1 Introduction

The use of the helium jet technique for the rapid transport of activities from a region of high background radioactivity to a much lower one has been quite successful. In most applications, room temperature helium gas has been used. This necessitates the use of some sort of macroscopic impurity or cluster in the gas to obtain useful transport efficiencies and in fact, quite impressive and even reproducible results (50% over ten meters) have been obtained with some impurities (Ma76).

The high transport efficiencies are understandable in terms of Bernouilli's equation for laminar flow. A radial pressure gradient exists that forces the clusters which carry the activity to remain in the center of the capillary over long distances.

Though the impurity-laden helium jet has shown its ability to transport activity over long distances and with high efficiency, these impurities may limit or even eliminate its use in certain applications. These include interfacing the helium jet to certain types of ion sources for mass spectroscopy, precise studies of β-spectra, high-resolution studies of heavy particle emission and

fundamental weak interaction studies which rely on the line shapes of β-delayed heavy particle lines.

It was found in 1974 by Äystö et al. (Ay74) that for "pure" helium cooled to liquid nitrogen temperatures (77°K) that a significant improvement in transport efficiency was possible relative to room temperature impurity-free helium jets (Ay73).

A model presented by Robertson et al. (Ro77) explains this behavior in terms of the thermal diffusion of active atoms through the carrier gas. This model assumes the loss of active atoms is due to collisions with the capillary wall which occur during their transport through the capillary. The increased efficiency is shown to be due in equal measure to the decrease in temperature (which decreases the rate of thermal diffision to the capillary wall) and to the increased molecular flow rate (which shortens the time the active atoms remain in the capillary).

In a paper by Robertson et al. (Ro77), the description of a cryogenic (liquid-nitrogen cooled) helium jet coupled to a recoil time-of-flight mass analyzer for use in observing short-lived β-delayed particle emitters was presented. This apparatus was used at Princeton University in an attempt to observe ^{24}Si. Results tentatively suggested that protons from the decay of this nucleus had been observed and that the mass of the T=2 state in the daughter nucleus ^{24}Al was consistent with the prediction from the quadratic form of the isobaric multiplet mass

equation. With these promising results, an improved apparatus was contructed here at Michigan State University with the intent of observing ^{24}Si and other T_z=-2 nuclei.

It is a feature of this apparatus that mass identification and background reduction can be obtained with only a single surface barrier Si detector (rather than a counter telescope) to detect the protons. The improved resolution and linearity, as well as the simultaneous recording of strong calibration groups, make possible a very precise measurement of the mass of the T=2 state in ^{24}Al. In addition, the first direct measurement of the half-life of ^{24}Si has been made. Figure 2-1 illustrates the β^+-delayed proton decay of ^{24}Si.

2.2 Beamline and beam transport

For these experiments a beam of 7Ø Mev ^{3}He ions from the Michigan State University Cyclotron produced ^{24}Si via the ^{24}Mg(^{3}He,3n) reaction. Figure 2-2 shows the beamline layout to the cryogenic helium-jet target chamber (located in vault 1). Also shown is the capillary feedthrough to the recoil time-of-flight apparatus (located in vault 5).

Beam position and focus were verified with a scintillator placed Ø.3 m in front of the target chamber. The beam passed through a 1.3 cm diameter aperture in each side of the target chamber and stopped in a water Faraday cup placed Ø.4 m past the target chamber. This Faraday cup was electrically isolated from the target chamber and the

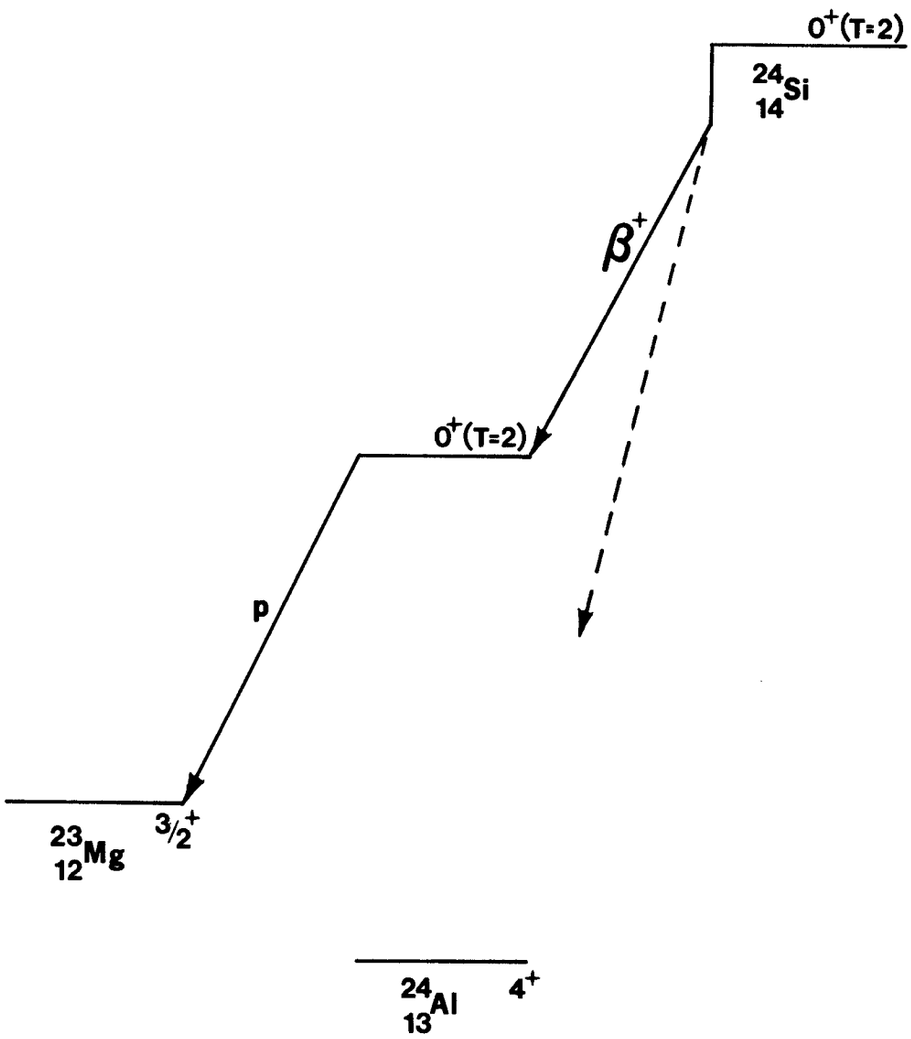

Figure 2-1. Illustration of the β^+-delayed proton decay of ^{24}Si.

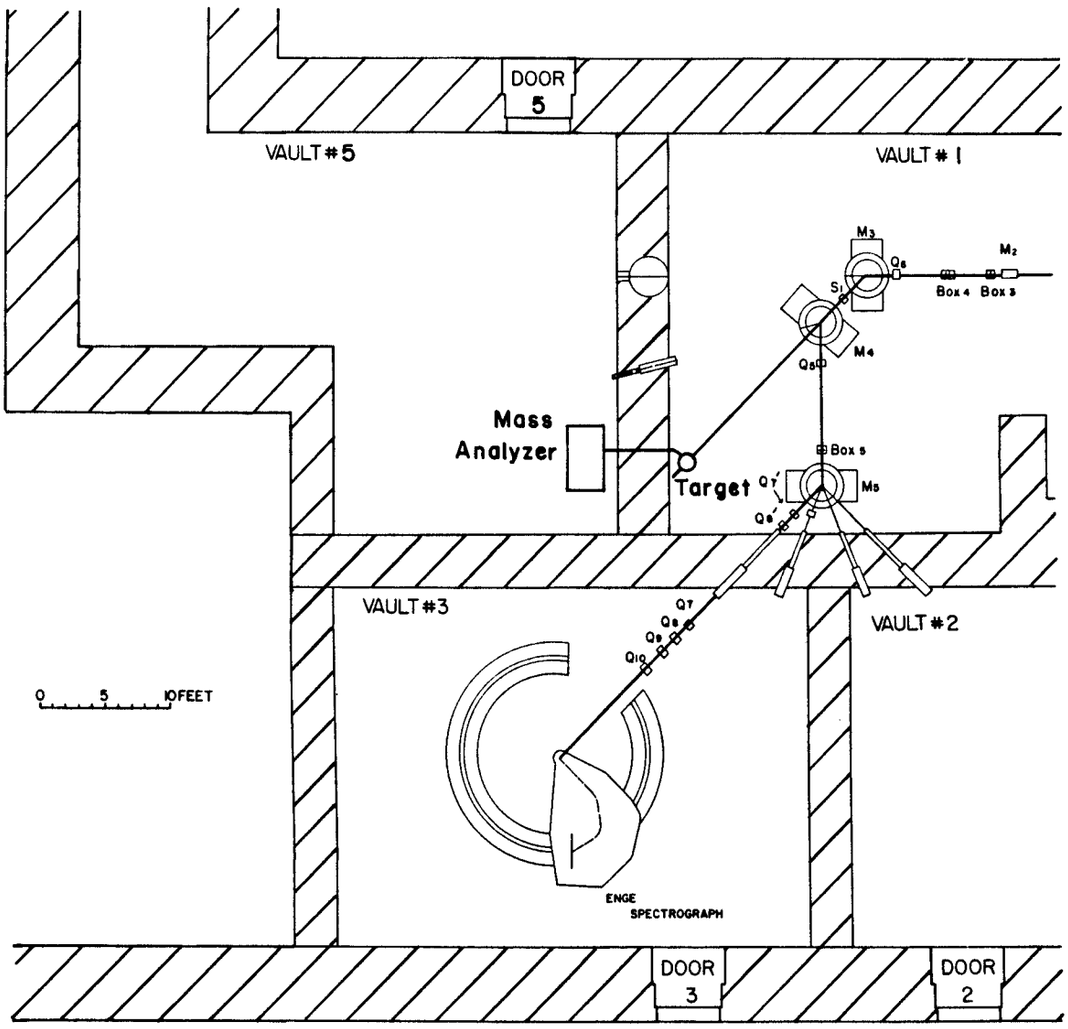

Figure 2-2. Beamline layout to target chamber.

rest of the beamline with an 8 cm section of insulating beam pipe. A current integrator gave both the total charge and the beam current. The beamline elements were adjusted to yield the maximum current from the Faraday cup. Depending on the tuning of the cyclotron, this current usually lay between 1 and 3 μA of $^{3}He^{++}$. Such currents did not lead to failures of the 5.25 mg/cm^2 Havar windows of the target chamber (Hi75). However, on one occasion, the windows ruptured after just three hours of 4-6 μA of beam current.

2.3 Helium jet target chamber

The helium jet target chamber consisted of a large (18 cm outer diameter x 35.5 cm long and 2.54 cm thick) aluminum tube, sealed at both ends with 1.3 cm thick aluminum cover plates. All flanges were sealed with indium wire.

The chamber was connected to the beamline by two stainless steel (5 cm outer diameter x 23 cm long and 1.7 mm thick) tubes, a 7.6 cm long section of which was turned down to a thickness of only ≅1 mm. This was done to minimize the heat loss through these tubes. The chamber was placed in a large (24 cm inner diameter x 46 cm inside depth) stainless steel dewar (Mv76) which was filled periodically with liquid nitrogen (LN_2). A LN_2 level controller (Nv76a) was used to keep the dewar full. A sensor placed ≅2Ø cm from the top of the dewar detected when the level of LN_2 went below this sensor. A solenoid valve then pressurized a feed dewar

which delivered LN_2 to the target chamber dewar for approximately three minutes. An insulating styrofoam cover was fit over the top of the dewar and target chamber and the stainless steel beamline connecting tubes were wrapped with a flexible styrofoam insulation. Figure 2-3 shows a cross-section of the target chamber.

Commercially "pure" He (99.995%) was sent at room temperature via 1/4 inch "poly flo" tubing to the vicinity of the target chamber where it connects to a 1.3 cm diameter copper tube of 2.5 m in length. As Figure 2-3 shows, this tubing was coiled about the target chamber and also placed in the LN_2 dewar. Thus, the He gas was cooled to $\cong$77°K before entering the target chamber. The gas entered through a porous stainless steel diffuser with 2 μm openings (Nu77). This prevented turbulence created by incoming gas which could significantly reduce the transport of activities (Ro77).

The target was mounted on a target holder which projected into the chamber as shown in Figure 2-4. The recoiling activities from the reaction of the beam in the target were thermalized (slowed down) in the cold He gas. In order to prevent the range of the recoils in the gas from exceeding the width of the target holder, the gas pressure was kept at approximately .7 atmospheres. Because of the increased gas density at 77°K, this pressure was sufficient to limit the range of the recoils to under 1 cm. The activities were then swept out of the chamber along with the

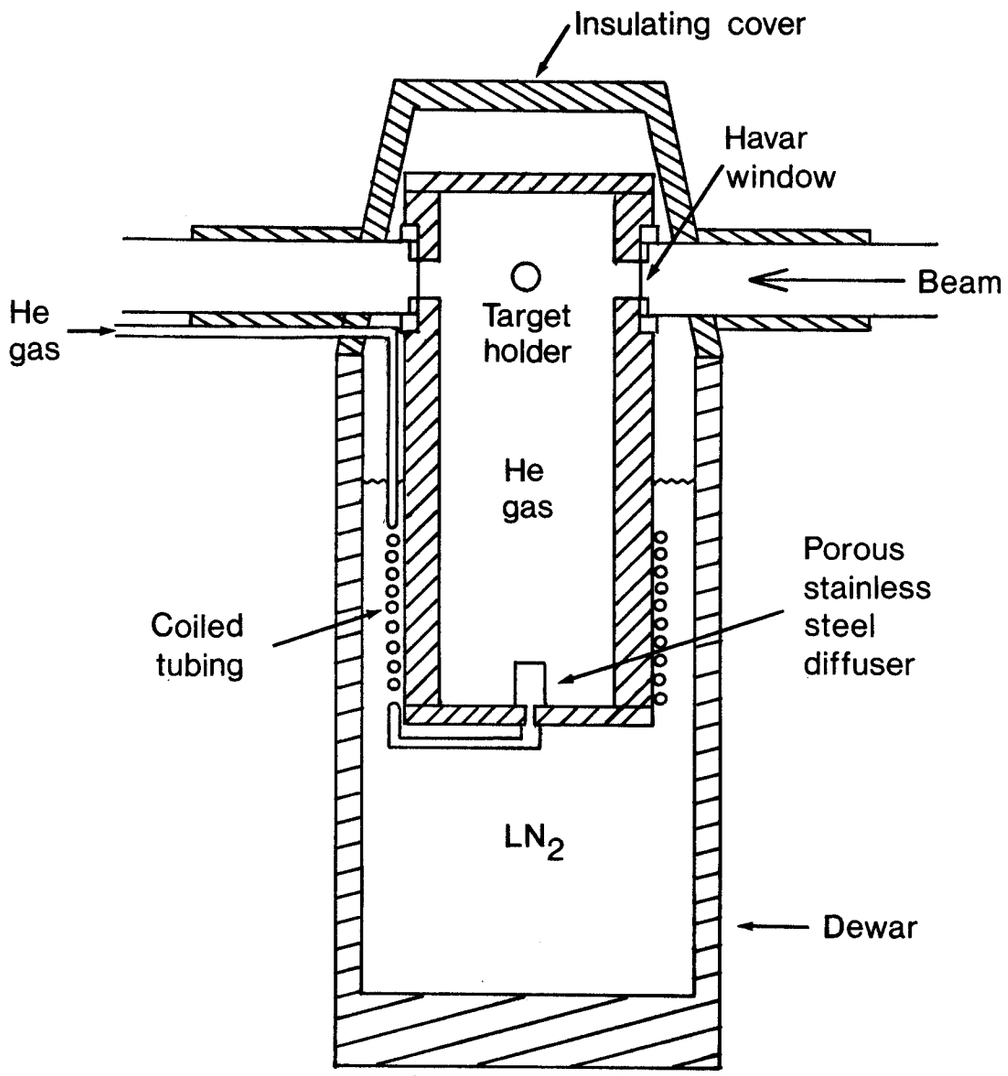

Figure 2-3. Cross-section of the target chamber.

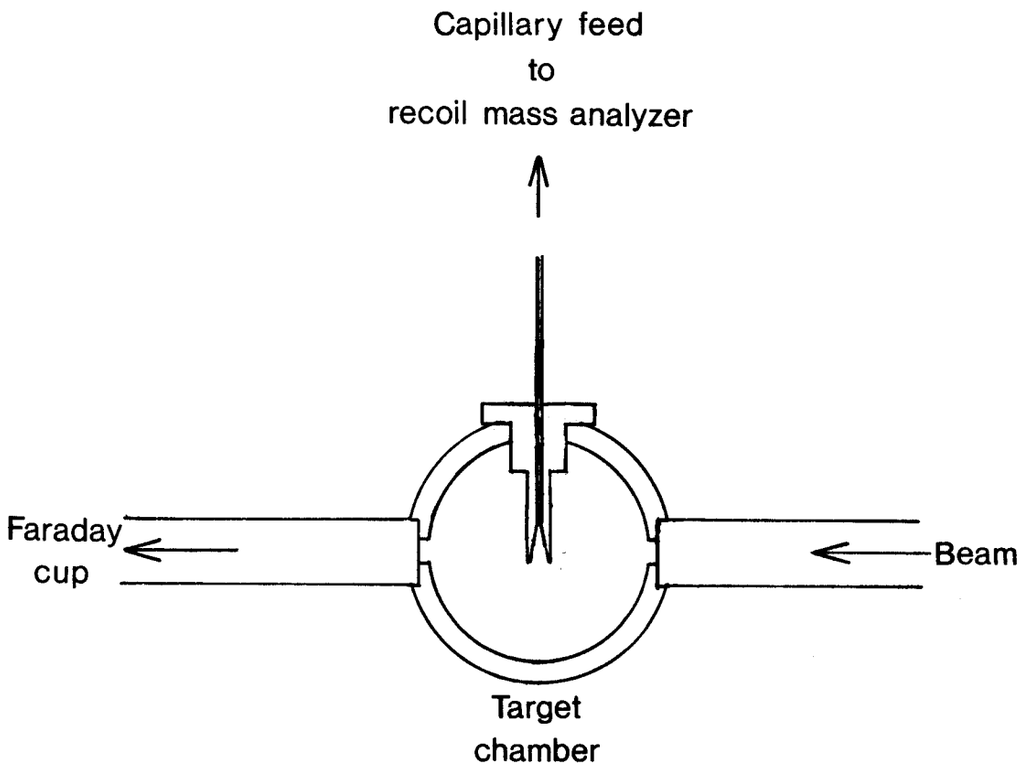

Figure 2-4. Top view of the target chamber.

He gas via a flared polyethylene capillary tube (1.8 mm inner diameter) and transported 2.4 m to the recoil time-of-flight mass analyzer.

2.4 Target holder and target

It was found by Robertson et al. (Ro77) that the target holder design was critical to the transport efficiency. Any turbulent flow behind the target reduced the transport of activities dramatically. Three target holder geometries were tested in this apparatus. Figure 2-5 shows views of the three configurations. Configurations A and C gave relatively similar results, but configuration B, which was a hoped-for improvement to configuration A, gave poor results. Configuration C was a later design which was used for the majority of the data collected. Transport efficiencies were on the order of a few percent.

The target used for these experiments was 5 mg/cm^2 of ^{24}Mg (99%) enriched that had been evaporated on a 2.3 mg/cm^2 copper backing.

2.5 Capillary-skimmer cone interface

The activity exited the capillary two to three millimeters from a skimmer cone. A 140 l/s Roots blower (Ro38) backed by an 80 l/s mechanical pump (Ki65) removed a large fraction of the He gas. Figure 2-6 shows this arrangement, along with a layout of the recoil time-of-flight mass analyzer system. The skimmer is a 90°

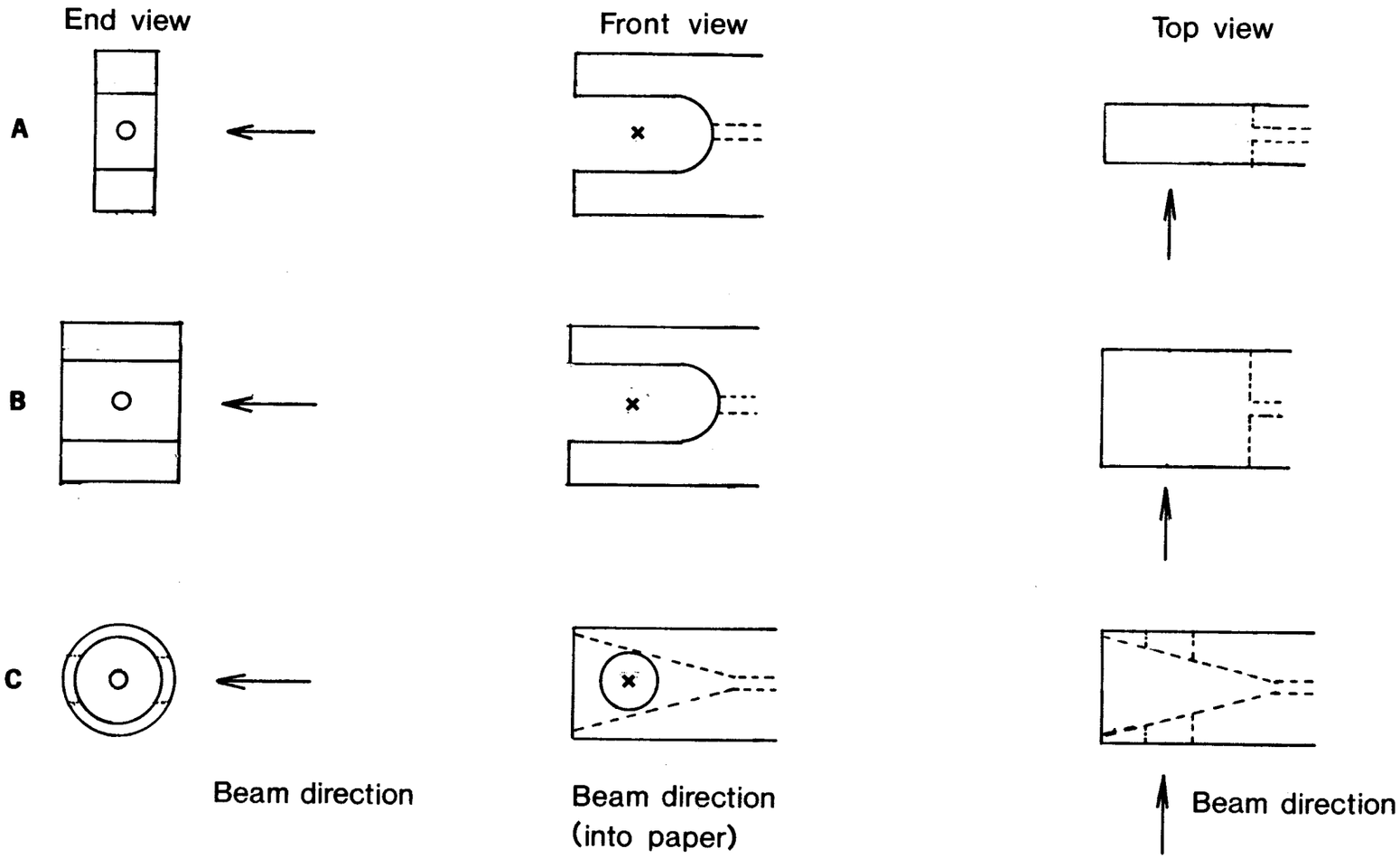

Figure 2-5. Three target holder configurations.

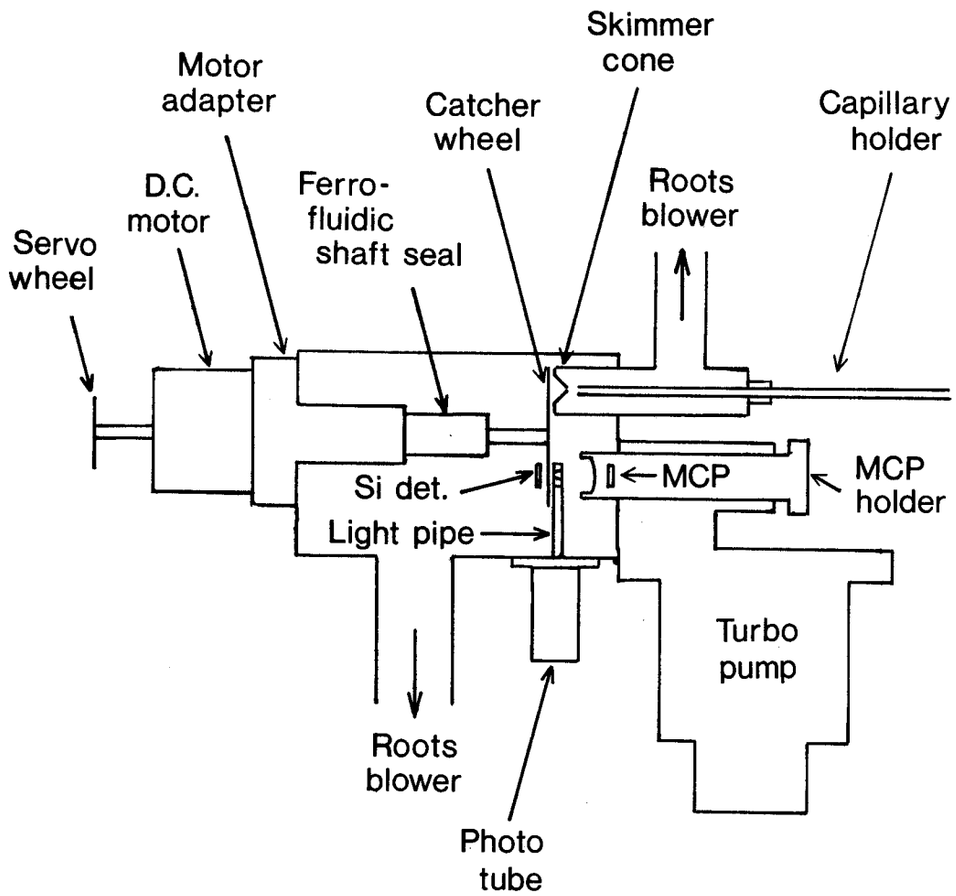

Figure 2-6. Layout of the recoil time-of-flight mass analyzer system.

cone with a 1.6 mm opening. The capillary is flared and seals against the o-ring on the end of a glass guide tube. This tube supports and also aligns the capillary with the skimmer opening.

During assembly the capillary is first flared on only one end (by holding vertically downward over a flame) and then fed through both the target holder and the shielding wall. After it is all the way past the end of the glass guide tube's seal, it is cut to length and flared. It is possible to move the recoil apparatus toward or away from the shielding wall where the capillary exits, allowing any slack to be taken up and the capillary put under tension.

2.6 Foil wheel and particle detection system.

The main chamber was pumped by a 150 l/s Roots blower (He61) backed by a 16.5 l/s mechanical pump (Va78) and a 25 l/s mechanical pump (We77) connected in parallel.

The transported atoms passed through the skimmer and into the main chamber, where they were deposited on a 10-12 $\mu g/cm^2$ thick, (6.4 mm diameter) Formvar catcher foil.

A vertically aligned foil wheel held six catcher foils. The foil wheel was stepped at a rate of 5 Hz with a high-torque hollow-rotor D.C. motor (Mi77). The wheel was connected to the motor by a Ferrofluidic shaft seal (Fe77). This seal allows for high shaft accelerations while maintaining vacuum integrity. Mounted on the opposite end

of the motor shaft, were a potentiometer (De78) and a small six-blade wheel. The potentiometer was used for recording the wheel position. The six-blade wheel (half the diameter of the catcher wheel) was part of the servo system for controlling the motor's motion. A linear filament light and a photodiode were mounted of opposite sides of the small blade wheel. The photodiode was part of a servo circuit which responded when the leading edge of the blade interrupted the light coming to the diode. This servo circuit controlled the motor which could keep the catcher foils locked into place between steps. The stepping rate was controlled external to the motor circuitry through a square wave generator.

The activity was allowed to collect for 200 ms, minus the approximate 20 ms stepping time. The wheel was then moved to its next position, where the newly-deposited activity was placed between the particle detectors (see Figure 2-7). After β-decay to particle-unstable states, both the particle emitted (proton or alpha) and the recoiling ion were observed in coincidence. Protons (or alphas) passed through the thin catcher foil and were detected using a single 150 mm^2, 300 μm deep Si detector (Or78). The residual nucleus is ejected from the surface of the foil. Figure 2-8 illustrates this arrangement.

The recoil ions have enough energy (160 keV for ^{23}Mg) to pass through a thin converter foil, placed opposite the Si detector. Secondary electrons from the converter were

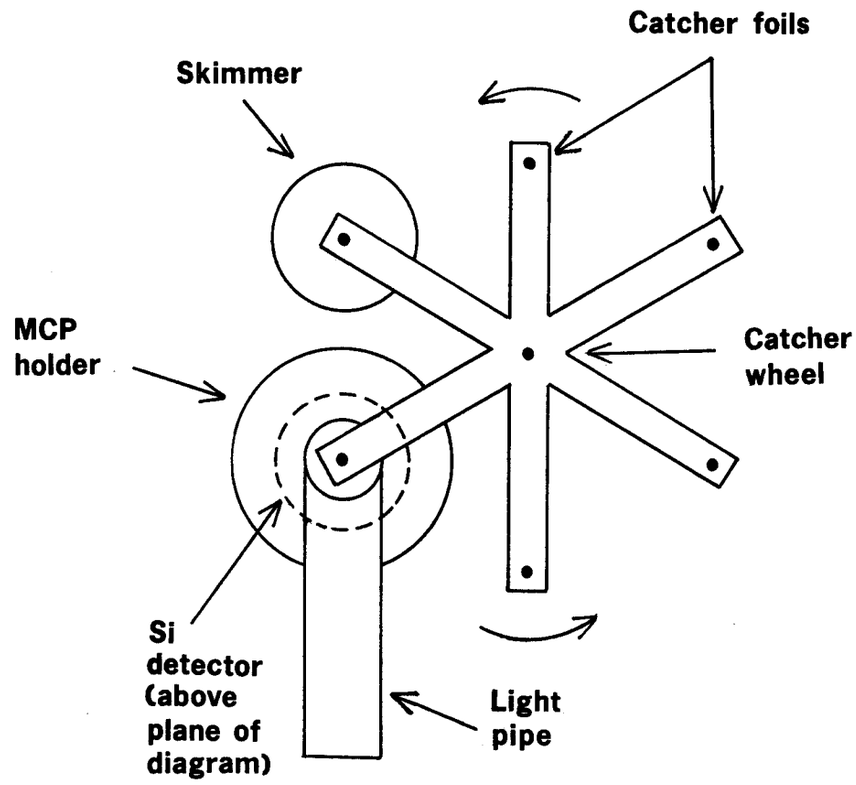

Figure 2-7. Front view of skimmer, catcher wheel and the detector system layout.

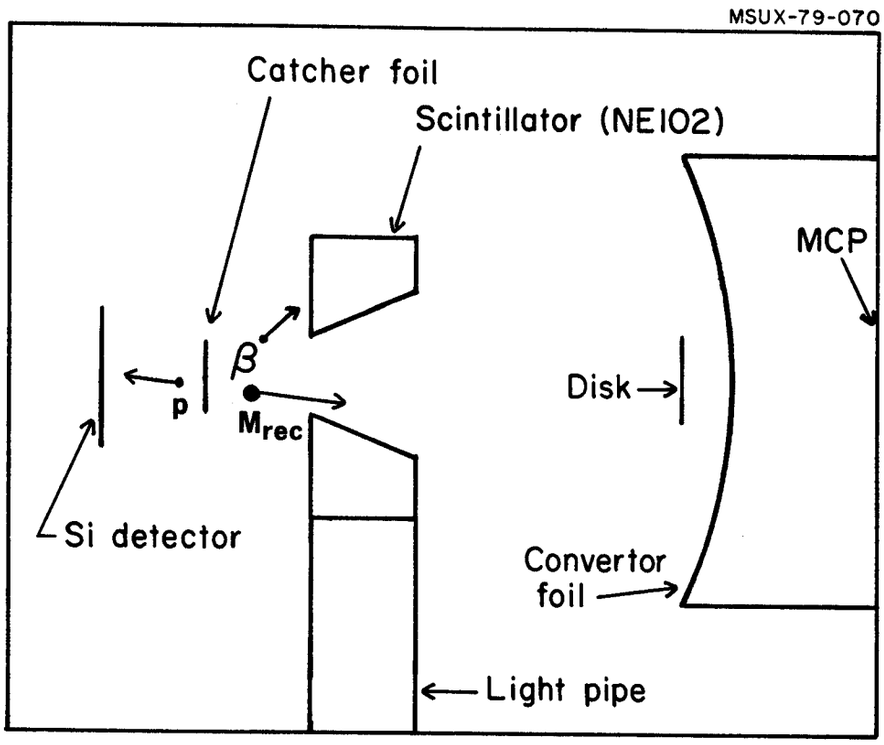

Figure 2-8. Cross section of detector region (not to scale). Activity was deposited on the right side of the catcher foil.

observed by a pair of Microchannel Plates (MCP) (Ga76). The 50.8 mm-diameter converter foil served also to isolate the MCP from the .14 torr pressure in the main detector chamber. This allowed the operation of the channel plates in a clean, high vacuum of 10^{-6} - 10^{-7} torr provided by a 1,500 l/s turbomolecular pump (Sa77).

The converter foil was shaped as a section of a sphere with an 80 mm radius of curvature. When placed 80 mm from the catcher foil, this curvature reduced the time spread of the recoil ions. Both the Si detector and converter foil subtended a solid angle of 2.6% of 4π. The converter foil consisted of a $\cong$30 $\mu g/cm^2$ layer of Formvar on a $\cong$95% transmission curved wire screen. The screen was made with 0.005 inch diameter copper wire layed onto a 80 mm radius convex wooden form. Onto the Formvar surface a $\cong$10 $\mu g/cm^2$ layer of gold and a $\cong$10 $\mu g/cm^2$ layer of CsI were evaporated. The layer of gold was used to prevent the converter foil from charging up. The CsI, with its higher secondary emission coeficient (Fa77,Bu77), was used to improve the detection efficiency of the recoils.

It may easily be shown (see Appendix A for a derivation of this result) that the mass of the recoil (daughter) nucleus M_{rec} is given by:

$$M_{rec} = \frac{\sqrt{2E_p m_p}\, t}{d} \qquad (2\text{-}1)$$

where t is the time of flight of the recoil mass, E_p the laboratory energy of the proton (or α), m_p the mass of the proton (or α) and d is the flight path (distance traveled by

M_{rec} during the time t). The recoil mass is proportional to t, not t^2 as in the usual time-of-flight system.

A start signal from the proton or alpha in the Si detector and a stop signal from the MCP gave a value for the time-of-flight of the recoil ion. This time, combined with the particle energy in the Si detector, was used in the above formula to derive the recoil mass.

The β-decay recoil determines the mass resolution in these measurements. For example, for ^{25}Si, which was produced in a competing reaction, this β-recoil limited the mass resolution to 7%, a value nevertheless adequate for mass identification. Appendix A also contains a discussion of this effect.

In initial experiments, it was found that the double coincidence data (between Si detector and MCP) showed two different recoil mass groups for the same particle energy. The second (slower) group was delayed by ≅9 ns and was attributed to recoil ions directly striking the MCP but failing to produce secondary electrons in the converter foil. In order to remove these ghost groups, which were producing a background in the region of interest, the design of an electrostatic lens was undertaken. It was hoped that a design could be found which would stop the recoils from striking the channel plates while still allowing the electrons to do so.

Lens designs were first modeled using the method of successive over-relaxation to solve Laplace's equation. See

Appendix B for a discussion of this method. A program was developed which allowed the testing of many different geometric configurations. This program also calculated particle trajectories through the lens.

A gridded lens design, illustrated in Figure 2-9, that focused the electrons to the central region of the channel plates was chosen. This design required only the central portion of the MCP to be used. The outer regions were masked off, and a small disk placed in front of the converter foil prevented the recoil ions from hitting the channel plates. A loss of only 7% in solid angle resulted from this arrangement, and a significant reduction in the background was achieved.

As in the previous apparatus (Ro77), an annular plastic scintillator was used to observe the initial β-decay of the parent nuclei. This scintillator was placed opposite the Si detector and subtended a solid angle of ≅37% of 4π. A plastic light pipe connected the scintillator to a photo-tube (Am77). Recoil ions traveled through a conical hole (20° half angle) in the scintillator to the converter foil. A cross-section of this scintillator is visible in Figure 2-8.

Many different activities are produced by the beam in the target and several delayed particle emitters were observed in our experiments. To make use of the mass identification capability, data was recorded in the event mode and, upon subsequent playback, proton and alpha energy

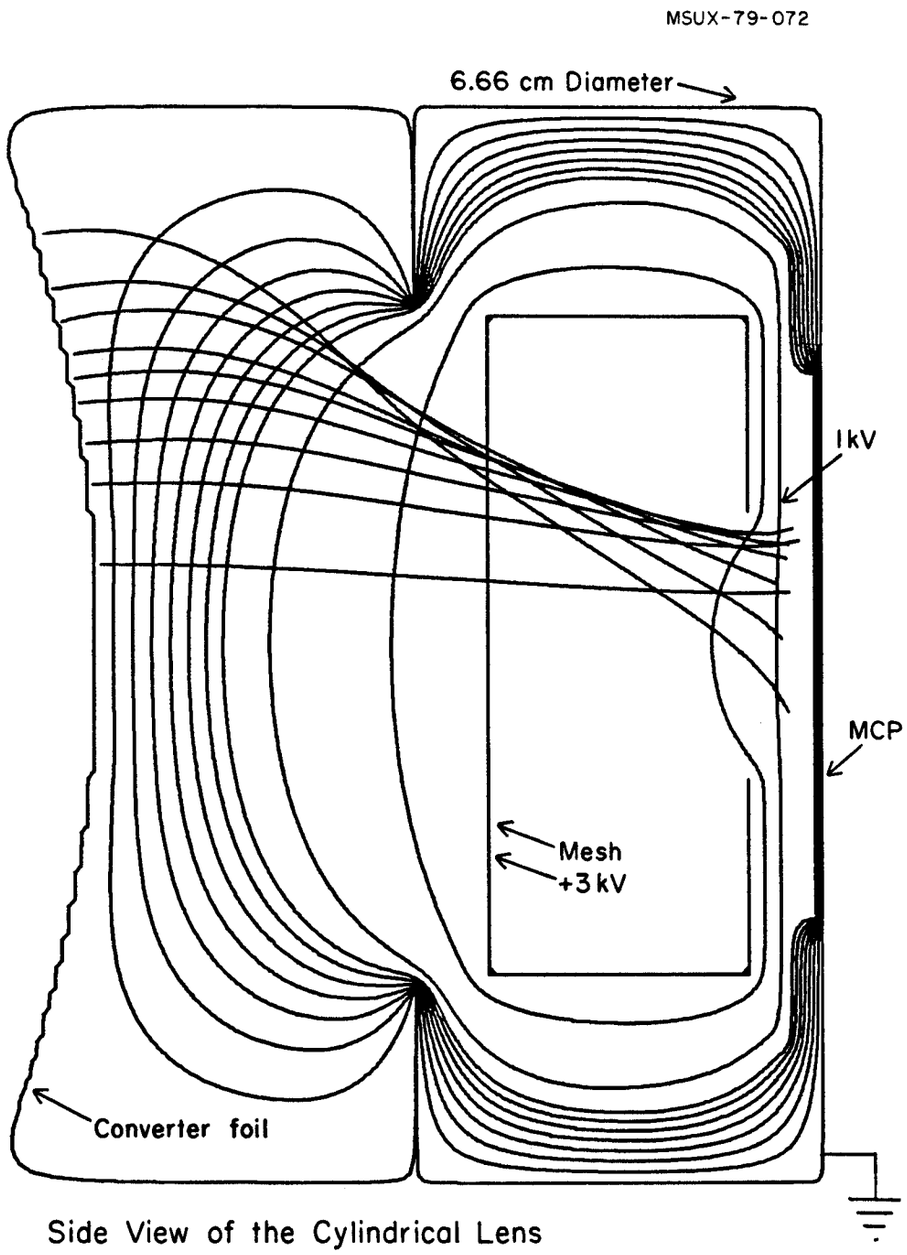

Figure 2-9. The model of the electrostatic lens, showing equipotentials and electron trajectories.